Deviation from Archie's law in partially saturated porous media: Wetting film versus disconnectedness of the conducting phase

M. Han,[1,2] S. Youssef,[2] E. Rosenberg,[2] M. Fleury,[2] and P. Levitz[1,*]
[1]*Physique de la Matière Condensée, Ecole Polytechnique, CNRS, 91128 Palaiseau, France*
[2]*IFP, Rueil Malmaison 92852, France*

(Received 4 August 2008; revised manuscript received 11 January 2009; published 30 March 2009)

We experimentally study the electrical transport in partially water-saturated pore network. The porous medium under investigation is a Fontainebleau sandstone, characterized by x-ray tomography. We show the existence of two electrical conductivity regimes. At high water saturation, the electric resistivity follows a well-known Archie law. Below a water saturation $S_w \sim 0.2$, a strong negative deviation from this Archie law is observed. We attribute this transition to the existence of "a thick liquid film," assuring the ionic conduction in the low saturation regime. A numerical simulation is proposed to confirm this scenario. Two possible protocols are used to distribute the brine phase in the pore network of a three-dimensional microtomography image. The first one is based on a minimization of the interfacial energy. The second takes into account a quasistatic capillary displacement. The classical random-walk algorithm is used to compute the electric conductivity at various water saturations. Without the "thick film," both of the two fluid-placing protocols show a disconnectedness transition of the brine phase when $S_w < 0.2$. Adding this "film" to solid surface, the electrical continuity is maintained. The bending down trend is correctly reproduced, showing that in this range, the electric response cannot be described by a power law as usual.

DOI: 10.1103/PhysRevE.79.031127 PACS number(s): 05.60.−k, 61.43.Gt, 05.40.Jc, 07.05.Tp

I. INTRODUCTION

The electrical properties of partially water-saturated rock have many applications in the geophysical science. In the petroleum industry, they are used to estimate the oil in place in a reservoir from the combined estimates of porosity and brine (conductive phase) saturation. The calculation of *in situ* saturation from resistivity logging data requires knowledge of the cementation exponent m and the saturation exponent n. The formation factor F_f and the resistivity index R_{ind} curves are usually described by power laws known as Archie's laws [1],

$$F_f = R_0/R_w = \Phi^{-m} \tag{1}$$

and

$$R_{\mathrm{ind}} = R_t/R_0 = S_w^{-n}, \tag{2}$$

where R_w is the brine resistivity, R_t is the resistivity of a system partially saturated by a conductive fluid, R_0 is the resistivity at full saturation, S_w is the volume fraction between brine and the total pore space, and ϕ is the porosity. Both m and n depend not only on porosity but also on details of the pore network. Moreover, plotting the R_{ind}-S_w curve cumulates important modeling and experimental difficulties related to the fluid distribution in the pore space, especially at low water saturation. Based on the data obtained on sandstones, the n default value in log analysis, in the absence of core measurements, is 2. However, it can vary typically from 1.5 up to 2.5. For giant reservoirs such as those encountered in the Middle East, the oil-in-place errors induced by different n values can represent 10 years of world oil consumption. There are several known reasons for the variation in n or the "non-Archie" behavior (non-nonlinear curves in log-log scale): the direct effect of the pore network structure and the wettability effect [2,3]. Our purpose here is to focus on water wet situation and to revisit a well-established idea that the electrical response on a clean sandstone should follow an Archie law with an exponent n close to 2. As will be seen, this may be not true at low water saturation in a very simple situation, and it is precisely in the low saturation range that the accurate estimation of n has large economical impact. Obviously, the detailed understanding in a simple water wet porous media has a direct implication in more complex situations such as those encountered in carbonate rocks that are of mixed wettability.

The brine-oil distribution in the pore space affects fundamentally the conductivity properties [4], which is the key issue to explain these non-Archie behaviors. However, the three-dimensional (3D) visualization and quantification of actual brine distribution in real rock samples remain a challenging experimental task [4]. As a result, the distribution of brine at pore scale as well as its role on the electrical conduction remains poorly understood. This is especially true for brine films. At low saturation for a water wet clay-free sandstone, a "thick film" in the solid roughness is often supposed to exist, providing the hydraulic continuity [5,6] in capillary dominated desaturation experiments. Although such thick films have little hydraulic conductivity and require time consuming experiments to drain, they may have a great influence on the electrical conduction. Nevertheless, there is little experimental data published about electrical responses at the low brine saturation range i.e., ≤ 0.20, partly due to experimental difficulties.

In this work, we present an extensive experimental analysis of the electrical response on a clean sandstone as well as a set of numerical simulations on a large saturation range.

*Corresponding author. FAX: +33 1 69 33 30 04; pierre.levitz@polytechnique.edu

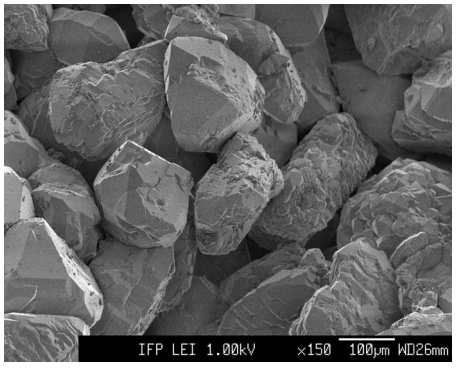

FIG. 1. Scanning electron microscopy (SEM) image of the Fontainebleau sandstone.

We propose a quantitative study about the thick-film influence on the electrical response. This paper is organized as follows. The first part provides the experimental data related to the electrical response of a Fontainebleau sandstone. Using 3D tomography reconstruction of the pore network [7,8], we then propose two possible ways to distribute the wetting phase inside the porous medium. We analyze their respective topology, especially their disconnectedness threshold at low S_w. In the last part, the electric transport is simulated using the random-walk algorithm [9–11]. Comparison with the experiment is performed. This last part shows the important role played by "thick wetting films" that provides the electrical continuity and explains the strong deviation from Archie law at low saturation level.

II. ELECTRIC RESPONSE OF A MODEL POROUS MEDIA

The sample studied is a Fontainebleau sandstone of porosity 0.22 and permeability of about 2100 mD. A key characteristic for our study is the absence of clay at the quartz grain surface as seen in Fig. 1. Although some apparent flat surfaces can be observed, most of the grains present a surface roughness. The electrical properties were measured using a 20 g/l NaCl solution (the brine). The formation factor is $F_f=12.4$. Using Eq. (1), the cementation exponent is estimated around 1.65. Other standard characterizations are also available; the specific surface area measured by krypton adsorption is 0.02 m^2/g. The dominant pore throat diameter determined by mercury injection is 40 μm, and the dominant pore (body) volume-to-surface ratio (V/S) determined by NMR is 7 μm (using a surface relaxivity of 5.6 μm/s [12]). The sample has a strong water wettability.

In the drainage cycle, different brine-air saturation states are obtained by horizontal centrifugation of the sample (length=3 cm, diameter=4 cm) at different speeds of rotation. More details can be found in a previous work [13,14]. In short, when a brine-saturated sample is centrifuged in air, a pressure gradient is generated by the centrifugal force. As a result, there is a saturation profile inside the sample. To avoid strong nonuniform profiles, we superimposed two plugs from the same core. The contact surfaces of the two plugs are smooth, and we added a thin water wet membrane between the contact surfaces to ensure a capillary continuity. We use a standard NMR one-dimensional (1D) imaging technique to observe the saturation profile along the cylinder axis. From the reference profile measured at $S_w=1$, the saturation profiles can easily be calculated from the amplitude ratio at a given position. In our study, the first plug exhibits, with a good approximation, a uniform profile along its axis (at the scale of the sample size). Moreover, the effect of the gravity [15,16] along a radial section can be neglected. This is due to the small pore size in our sample. Based on the mercury injection and the image analysis, the mean size of the pore throat is about $r_c=20$ μm. The capillary pressure P_c at the beginning of the drainage is about $P_c=2\gamma/r_c$ where $\gamma=72\times10^{-3}$ N/m is the interfacial tension of the water-air interface. P_c is found equal to 7200 Pa. The pressure due to gravitation buoyancy is about $P_g=(\rho_{\text{water}}-\rho_{\text{air}})gh$ where $\rho_{\text{water}}=1000$ kg/m^3 and $\rho_{\text{air}}=0$ kg/m^3 are the density of the water and the air. $g=9.8$ m^2/s is the acceleration of gravity and $h=0.04$ m is the sample diameter. Taking these values into the former equation, we get $P_g=390$ Pa. As $P_g \ll P_c$, the gravity effects stay negligible even at the beginning of the drainage.

After each centrifuge period, the amount of brine in the sample is measured by weight as well as by NMR to avoid errors due to potential grain loss. The electrical resistance is measured in a core holder cell in which electrodes are implemented radially around the sample. A four-electrode configuration is used (voltage is measured using electrodes different from those used for current injection) to avoid contact resistance between the sample and electrodes. A moderate pressure is applied on the electrodes to ensure that the electric field is the same from one measurement to another. The resistivity index is obtained from the ratio of the resistance at a given saturation to the resistance at $S_w=1$. We also paid attention to potential errors induced by drying during centrifugation. During centrifugation, separate tests performed at constant saturation indicate no drying. During electric measurements, sample weight control before and after indicated negligible drying. To increase the saturation (spontaneous imbibition cycle), the sample is placed in a beaker with a given amount of brine in order to reach the desired saturation.

The R_{ind}-S_w curve measured in drainage and imbibition on the Fontainebleau sample is shown in Fig. 2. In primary drainage, we can distinguish two different resistivity regimes; when the brine saturation is greater than about 0.2, the data point agrees with a power law with an exponent n close to 1.9; below this 0.20 threshold, we observe a negative deviation and the n value diminishes locally toward 1.4. In imbibition, the pores previously emptied by air are refilled by brine. When $S_w<0.4$, the drainage and imbibition data points are superimposed, while above 0.40, the R_{ind} curve in imbibition is slightly below the drainage. This result is repeatable and is coherent between the measurements performed on different plugs of the same rock. In drainage, our experimental results for $S_w>0.20$ are in agreement with other measurements on clay-free sandstones [17,18]. However, the bending down behavior at low S_w is much unexpected and this trend is rarely discussed in literature.

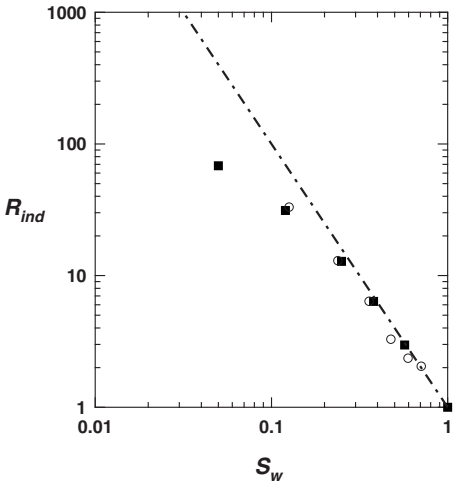

FIG. 2. R_{ind}-S_w curves of the Fontainebleau sandstone in drainage and imbibition modes. Black square: measurement in drainage mode. Circles: measurement in imbibition. Dotted line: Archie law [Eq. (2)] with $n=2$.

III. 3D TOMOGRAPHY OF THE POROUS MEDIUM

The 3D microtomography was performed with a Nanotom from PHOENIX X-Ray. The source is generated by the impact of a focused electron beam on a thin target. Spot size varies between 1 and 5 μm depending on operating conditions (less than 2 μm in the conditions used). The diverging geometry of the x-ray source results in a magnification of the object image. The detector is a Hamamatsu flat detector (110×110 mm^2) made of 2304×2304 pixels 50 μm large, a magnification of 16.7, thus allowing a pixel size of 3 μm on the radiographs. Generating 3D images starts with the acquisition of a series of two-dimensional (2D) projections while progressively rotating the sample step by step through a full 360° rotation at increments of less than 1° (0.2° for 1800 projections). Acquisition parameters are the following: sample diameter of 5.5 mm, source object distance of 12 mm, source-detector distance of 200 mm, pixel size of 3 μm, 2304×2304 field of view, 90 KV, 170 μA, 0.2° angular step, Cu 0.1 μm filter, and 2 h 30 min. acquisition time.

Most of the imaging work was performed on the dry sample. One experiment was conducted on a partially water-saturated pore network. An example of a dry sample is shown in Fig. 3. After a segmentation step, the porosity of the 3D volume is 0.21. The specific surface of the numerical medium is 0.0158 m^2/g. We have computed the two point correlations of the pore network. This function reaches a plateau for a correlation length of about 130 pixels, about four times less than the size of the configuration shown in Fig. 3. This correlation length gives a good approximation of the representative elementary volume size.

IV. NUMERICAL SIMULATION OF THE FLUID DISTRIBUTION IN 3D PORE NETWORK

For modeling the electrical property in a partially saturated media, the first task is to distribute the conductive phase in the porous space. We propose here two methods: (1) the simulated annealing and (2) the quasistatic capillary displacement.

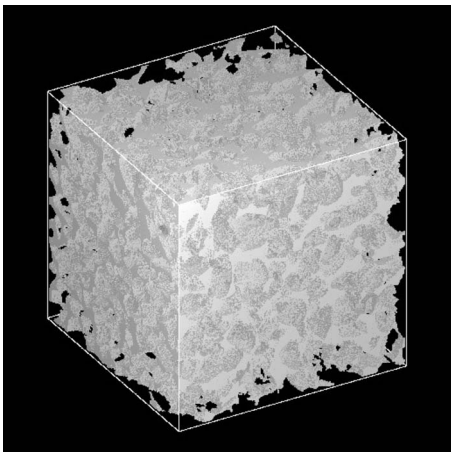

FIG. 3. 3D microtomography of the dry Fontainebleau sandstone pore network. The size of the cube is 1.5 mm (500×10^3 voxels).

A. Simulated annealing

Several researchers have experienced the simulated annealing method [19] to study the water-air distribution in soils and rocks. Knight *et al.* [20] at first used this method in a 2D digitized thin section image of Berea sandstone to find the equilibrium phase distribution. The principle is based on the assumption that the distribution of fluid phases is governed by the static interfacial free energy of the system, such that the equilibrium phase distribution corresponds to a minimum in the total interfacial free energy of the system. She concluded that the simulated annealing had been successfully applied to the problem of determining an equilibrium fluid distribution in a porous medium. However, this method cannot be used to distinguish different saturating processes, such as the drainage or imbibition. A similar extension to three dimensions was used by Silverstein and Fort [21] to investigate fluid distributions in sphere packs. Berkowitz and Hansen [4], to our knowledge, were the first to apply this method directly on the tomography 3D image. Their calculations provided important insight into how water is distributed in a partially saturated porous rock. Estimates of relative interfacial areas among water, air, and solid phases can be used as input to models that account for chemical exchange and reaction across these interfaces. They indicated that the assumption of equilibrium distribution in rock's pore network "may be reasonable, in particular, for water distributions at low saturation."

In the following, our aim is to implement a simulated annealing algorithm allowing one to minimize the global interfacial energy. A number of water voxels corresponding to a prescribed saturation are placed randomly inside the pore space, providing an initial distribution of water and air, as shown in the top part of Fig. 4. The optimal placement of these voxels is then found by using the Metropolis algorithm. The Metropolis algorithm is an integral component of the

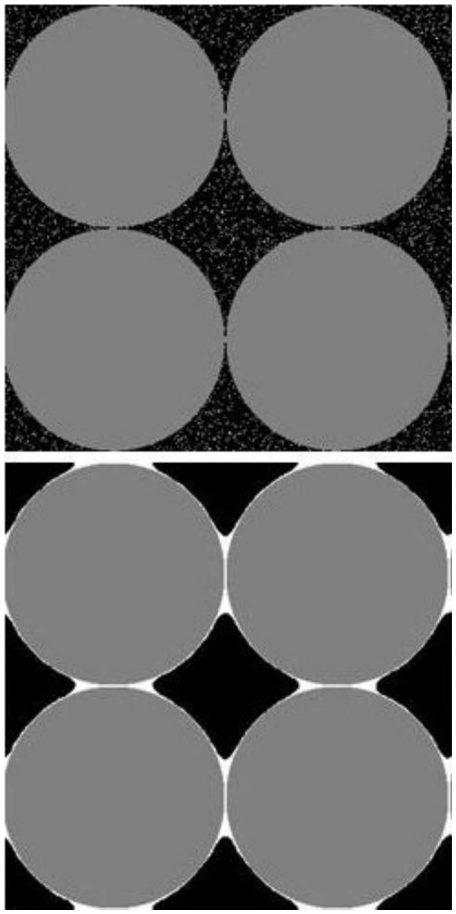

FIG. 4. Computation of the capillary condensation in a cubic structure composed of eight spheres using simulated annealing algorithm: (a) initial state and (b) final state.

simulated annealing method [22]. Changes in the system are randomly generated and an energy change, δE, is calculated. If $\delta E \leq 0$, the change is allowed, otherwise the probability of the change accepted is calculated using the Boltzmann probability distribution,

$$P(\delta E) = \exp(-\delta E/T_{\text{eff}}), \tag{3}$$

where T_{eff} is an effective temperature. The value of $P(\delta E)$ is compared to a random number R between 0 and 1. If $P(\delta E) > R$, the change is allowed, otherwise, it is refused. At each effective temperature, vapor and water elements are selected randomly and swapped. δE is calculated by considering the change in interfacial energy of each element. In this work, the 26 nearest neighbors are considered for the interfacial energy calculations. The values for the interfacial free energy used are $\gamma_{\text{LV}}=72$ m Jm^{-2}, $\gamma_{\text{SV}}=422$ m Jm^{-2}, and $\gamma_{\text{SL}}=350$ m Jm^{-2} for the interfaces liquid-vapor, solid-vapor, and solid-liquid, respectively [4,20]. Starting at a high value T_0, T_{eff} diminishes progressively by a factor α. At each temperature step, an amount of the water-air voxel pairs corresponding to twice the total number of pore voxels are chosen and swapped. The Metropolis algorithm is used at each exchange until the system reaches its minimum state of global energy. The cooling schedule parameters, determined by trial and error, were set at $T_0=1000$ and $\alpha=0.9$. These values were determined under the rules suggested by Kirkpatrick *et al.* [19].

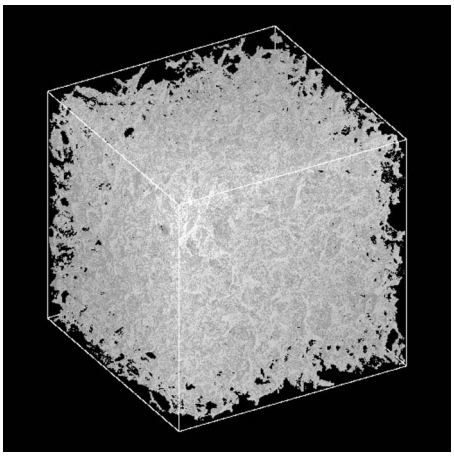

FIG. 5. 3D reconstruction of the water distribution inside the Fontainebleau sandstone pore network at $S_w=0.3$ using a simulated annealing algorithm. The size of the cube is 1.5 mm (500×10^3 voxels).

First of all, we have tested our simulation program in a simple-cubic structure composed of eight spheres with a water saturation $S_w=0.05$. The system is discretized by 400×10^3 voxels. The results are in good agreement with the experimental observations shown by Dullien *et al.* [23] where the water elements are found either at the grain contacts forming the menisci or in a film covering the solid surface, as shown in Fig. 4. The simulated annealing algorithm is used to partially fill the pore network shown in Fig. 3 at 0.05, 0.1, 0.15, 0.20, 0.31, 0.41, and 0.62 brine saturation. An example of a 3D distribution of brine is shown in Fig. 5. At the scale of the 3D microtomography reconstruction, the brine distribution is uniformly distributed.

Experimentally, it is far too easy to get a quantitative analysis of the air-water distribution inside the pore network by x-ray tomography. However, such an experiment was achieved in one case as shown in the top part of Fig. 6. One of the drained samples has been transferred to a closed vessel of the x-ray tomography. The acquisition time was 1 h. Three regions are clearly visible: the solid matrix, the empty pore network, and the capillary water phase. The volume fraction of this last phase corresponds to a value $S_w=0.27$. Clearly, the water phase is located on the highly curved parts of the pore network surface. The corresponding numerical simulation at $S_w=0.3$ is shown in the lower part of Fig. 6 and a similar brine configuration is observed. Brine elements are initially added to the system around the contact points of the grains, called menisci; at some higher brine content, the smaller pores are completely saturated by brine elements; as the saturation increases, the menisci develop whereas the biggest pore centers remain air filled. These results are in good agreement with the former numerical work of Silverstein and Fort [21]

The box-counting method has been used to analyze the fractal properties of the displacement structures. For this, we count the number of cubes $N(\varepsilon)$, having a size ε, needed to

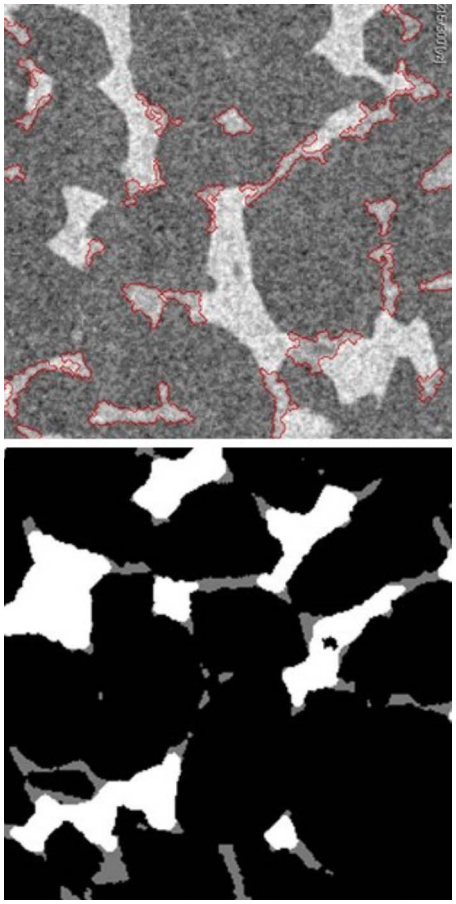

FIG. 6. (Color online) On the upper part: a section of a 3D microtomography of a partially water-saturated pore network (S_w =0.3). The water phase appears in medium gray level. The part below: water distribution inside the pore network at S_w=0.3 using a simulated annealing algorithm (see text). The solid is in black, the water phase is in medium gray, and the empty pore network is in white.

cover either the nonwetting or the wetting phase. It is well known that in a scaling regime, $N(\varepsilon) \propto \varepsilon^{\bar{D}}$ where $\bar{D}$ is the fractal dimension. The evolution of $N(\varepsilon)$, relative to the wetting phase, is shown in Fig. 7, for S_w ranging from 1 to 0.05. The fully saturated pore network (S_w=1), exhibits two scaling regimes. For $\varepsilon < 30$ pixels (i.e., 90 μm), a first algebraic dependence is observed with an exponent $\bar{D}$=2.5. This regime appears at the scale of individual grains of the Fontainebleau sandstone (see Fig. 1) and reflects the complex local pore geometry. A homogeneous repartition is observed for $\varepsilon > 30$ pixels with $\bar{D}$=3. For a saturation level lower than 1, the first regime evolves and we observe a decrease in the exponent ($\bar{D}$=2 for S_w=0.20, $\bar{D}$=1.8 for S_w=0.15, and $\bar{D}$=1.5 for S_w=0.05). Meanwhile, the crossover to the 3D homogeneous distribution appears always at the same characteristic size, about ten times less than the system size. In such a situation, finite-size effects should be weak even at low S_w.

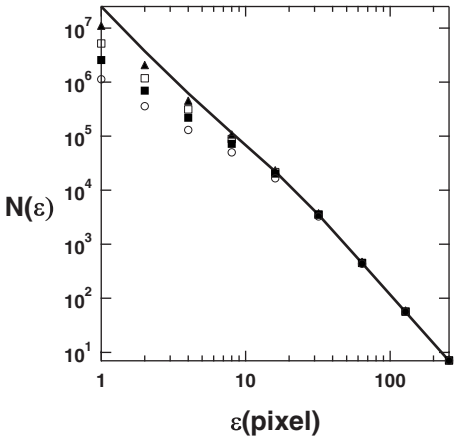

FIG. 7. Box-counting data for wetting fluid distribution obtained by a simulated annealing. Full line: S_w=1. Full triangle: S_w=0.40. Open square: S_w=0.20. Full square: S_w=0.10. Open circle: S_w =0.05.

B. Quasistatic capillary displacement

The drainage is generally considered to be controlled by capillary pressure at the pore scale [6,24,25]. Modeling the drainage process by the quasistatic displacement in this work is based on the pore space percolation by capillarity, where the viscous effect is neglected. Many studies of this type have been undertaken on two or three-dimensional lattices, the nodes and bonds of which represent the pore bodies and pore throats [26,27].

In our simulation, the fluids are displaced directly on the real pore space obtained by tomography. The parameters of the pore space are extracted locally on the image [28], such as (1) the partition of the elementary pore bodies; (2) the radius of the pore throats r which correspond to the pore space constrictions, so the capillary pressure of each throat can be given by the Laplace law; (3) the list of the neighborhood among the pore bodies (between two pore neighbors, there should be at least a throat providing their connection). In drainage, the pore space is initially fully filled with brine saturation. Then the nonwetting phase is forced to penetrate the media along one direction through the inlet face under a small differential pressure, whereas the outlet face allows only the passage of the wetting fluid but stops the nonwetting fluid. As the applied pressure is increased by small increments, the nonwetting fluid penetrates first only in the largest pores having a small capillary pressure value. The fluid displacement in the pores is immediate and complete. The applied pressure increases progressively until the smallest pores are penetrated. During the filling, the wetting phase can be cut off by the displacing fluid, and hence can be trapped. The brine configurations are computed at $S_w \doteq$0.06, 0.14, 0.28, 0.43, 0.56, 0.66, 0.78, and 0.79. Figure 8 shows one example of the brine distribution in 3D at S_w=0.3. We can observe brine aggregates isolated by air. Clearly the brine distribution is not homogeneous in space. This is because in our work the porous media size is near the minimum needed for simulating the two phase flow, as suggested by Dullien [6]. The boundary effects become too important (the pores at the cube surface have less connectivity). In addition,

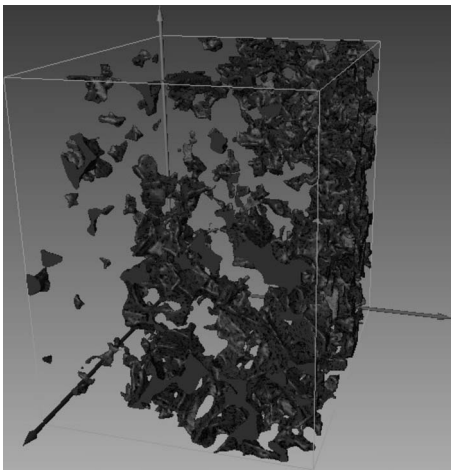

FIG. 8. 3D visualization of the brine configuration at $S_w=0.28$. The brine is invaded by air along the X axis. We can find the small brine aggregates isolated by air. The largest size of the box is 1.5 mm ($500\times500\times400$ voxels).

our simplified drainage algorithm does not leave menisci behind the displacement front.

Again, the box-counting method has been used to analyze the fractal properties of the displacement structures. As shown in Fig. 9, the nonwetting phase is length-scale invariant on more than 2 orders of magnitude, with a fractal dimension $\bar{D}=2.5$. $\bar{D}$ does not change with S_w. $\bar{D}=2.5$ is in good agreement with the expected fractal dimension of 3D invasion percolation [29].

Evolution of $N(\varepsilon)$ relative to the wetting phase is shown in Fig. 10 for S_w ranging from 1 to 0.06. For $S_w<1$, a complex evolution appears. Two main regimes are observed. First, for small ε values, we retrieve a $\bar{D}=2.5$ regime, characterizing saturated pores at small scale. The range where this regime is taking place gradually shrinks as S_w decreases. It is progressively replaced by an intermediate regime with a larger extension. We attribute the emergence of this second

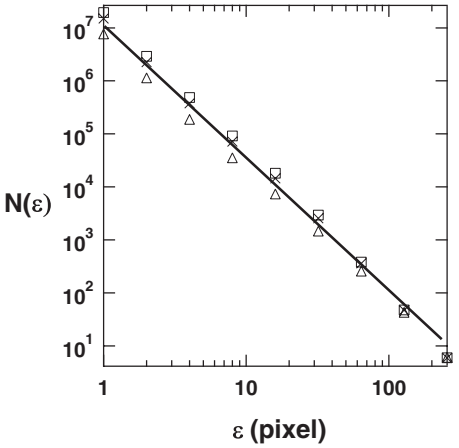

FIG. 9. Box-counting data for the nonwetting fluid distribution obtained by a quasistatic capillary displacement. Open triangle: $S_w=0.65$. Cross: $S_w=0.26$. Open square: $S_w=0.06$. The full line provides a guideline following an algebraic law with $\bar{D}=2.5$.

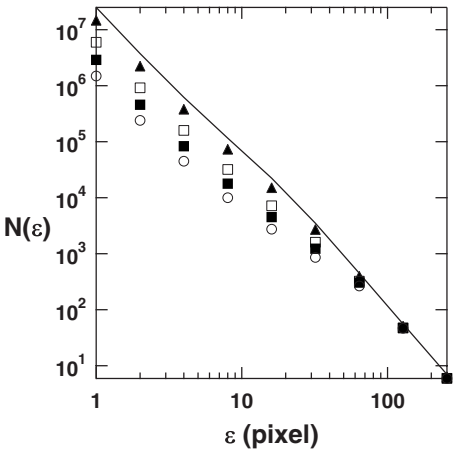

FIG. 10. Box-counting data for the wetting fluid distribution obtained by a quasistatic capillary displacement. Full line: $S_w=1$. Full triangle: $S_w=0.65$. Open square: $S_w=0.26$. Full square: $S_w=0.13$. Open circle: $S_w=0.06$.

regime to the trapped regions, made of wetting fluid, within the span front and exhibiting a heterogeneous and/or a fractal structure [25] on a length scale equivalent to the 3D reconstruction size.

C. Topology and connectedness of the wetting fluid

Diffusive, electric, and convective transports strongly depend on the topology of the wetting fluid inside the pore network [31–33]. In order to characterize the connectivity of this phase, we have computed its 3D skeleton graph [34]. This graph, defined as a set of vertex and links, is obtained after a thinning skeletonization statistically centered in the fluid phase and conserving the three Betty numbers (the number of connected parts, the number of irreducible paths, and the number of irreducible internal surfaces). In order to limit the artificial roughness related to the binarization of the image, we have first eliminated finite brine aggregates having less than five voxels. Second, we have computed the skeleton graph without termini (dangling bonds that are eliminated under a continuous retraction). A visualization of such a graph of retraction is shown in Fig. 11. The statistical distribution of links around a connected vertex [the so-called degree distribution $P(N_c)$] is shown in Fig. 12. In this curve, we did not take into account isolated vertexes, reminiscent of simply connected aggregates and having an Euler-Poincaré invariant $N_3=1$. All probability density functions evolve exponentially with N_c. As expected, we notice a strong similarity between the degree distributions characterizing the static capillary displacement and the saturated pore network. The network associated to the capillary condensation appears more connected, exhibiting larger N_c values.

In order to characterize, in a simple way, the evolution of the 3D skeleton graph, we propose to consider the following number:

$$C=-\frac{(\alpha_0-\alpha_1)}{\alpha_0}, \tag{4}$$

where α_0 is the total number of vertexes (isolated or not) and α_1 is the number of links. The definition of C allows one to

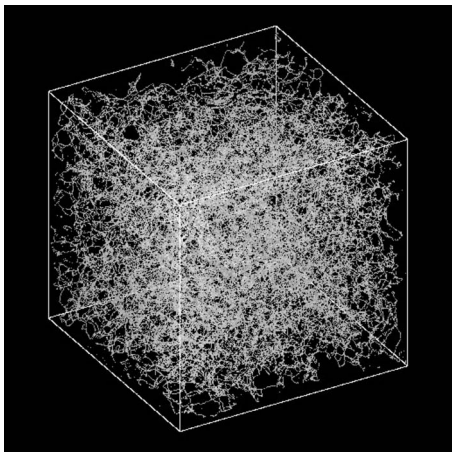

FIG. 11. 3D visualization of the graph of retraction of the water phase computed using simulated annealing algorithm at $S_w=0.30$. The size of the cube is 1.5 mm (500×10^3 voxels).

define an *intensive* characteristic related to the number of irreducible paths per vertex.

For a graph without isolated vertexes, it is straight forward to check that

$$\langle N_c\rangle = 2(C+1), \tag{5}$$

where $\langle N_c\rangle$ is the first moment of the probability density function $P(N_c)$. C is then essentially positive. The higher its value, the more connected is the pore network. For a disconnected pore network with a large number of dissociated parts, a great number of isolated vertexes emerge and α_0 dominates in the right part of Eq. (4). In such a case, C is negative, ranging between 0 and −1. Equation (5) can be rewritten in a similar way but with a redefinition of $\langle N_c\rangle$ as the first moment of a probability density function $P_T(N_c)$ which includes the occurrence of isolated vertexes.

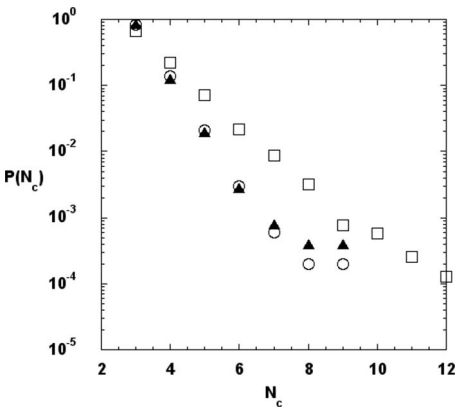

FIG. 12. Evolution of the distribution of the number of connections (the degree distribution) of the retraction graphs associated to the fluid distribution obtained either by a simulated annealing or by a quasistatic capillary displacement. Open circles: saturated pore network. Full triangles: Pore network saturated at $S_w=0.28$ under static capillary displacement. Open square: capillary condensation of the pore network at $S_w=0.3$ computed with a simulated annealing algorithm.

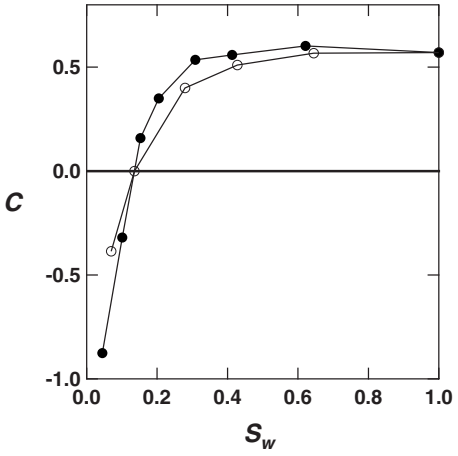

FIG. 13. Evolution of the topological constant C [Eq. (4)] with the degree of water saturation. Open circles: static capillary displacement. Full circles: capillary condensation of the pore network computed with a simulated annealing algorithm.

Evolution of the topological constant C with the degree of water saturation is shown in Fig. 13 for the static capillary displacement and the simulated annealing. Above $S_w=0.2$, the first scenario exhibits a more connected wetting phase. The location where C gets null, around $S_w=0.12$, is an interesting region where we also observe a zero crossing for N_3. As discussed elsewhere by several authors [11,35–37], the null N_3 value corresponds to a hyperbolic/elliptic interface transition linked to a percolation transition. To the best of our acknowledge, there is no mathematical proof of this coincidence. However, it is encountered in several random pore networks [35], for example, generated using a correlated Gaussian random field [11,36].

D. Discussion

To sum up, let us recall the advantages and the disadvantages of the two numerical methods. For the capillary displacement method, the brine displacement is controlled by the capillary pressure, which captures the principle of the oil migration in the reservoir. Nevertheless, its principal disadvantage is that it neglects the dynamical effects, whereas the viscous pressure drop plays a key role in the biphasic displacement. What is more, in this work, is that the pore network of the tomography image is only composed of 5072 "nodes," which is near the minimum needed for this type of convective transport. The "simulated annealing" method describes correctly the menisci at the grain contacts. The brine distribution is isotopic and the saturation profile is uniform. It seems to represent well the brine configuration after drainage at saturation range <0.4, where the brine is known to situate in the grain contact points and the smaller pores [40]. However, at $S_w=0.62$, we numerically observed a discontinuity of the nonwetting phase. This is contrary to the general drainage process that the nonwetting phase is never isolated. The brine configuration at 0.62 seems more similar to an imbibition process, and the isolated nonwetting phase signifies the "snap-off" phenomena.

V. ANALYZING ELECTRIC CONDUCTIVITY FROM 3D IMAGES

A. Method

The electrical response is calculated by the "random-walk" method. The media is the 3D tomography image containing the brine phase obtained previously. At each fluid configuration, 10000 walkers are dropped randomly in different brine voxels and then move randomly to one of its 26 neighboring voxels. If this neighbor is filled by the brine phase, then the movement is allowed. The displacement r is added by Δr and the diffusion time t is also added by Δt. Otherwise, its last displacement is not countered and the walker turns back to its previous position; however the diffusion time is still added. From Einstein's relation, $r^2=6Dt$, the slope of the mean-square displacement r^2 over all walkers at long diffusion time t $(t\to\infty)$ gives the effective self-diffusion coefficient, $D_{\text{self}}(t\to\infty)$, of the walkers inside the pore space. $D_{\text{self}}(t\to\infty)$ is proportional to the electrical resistivity. The formation factor and the resistivity index can be calculated by Eq. (6) where D_{bulk} is the self-diffusion coefficient of the free liquid water. Note that the tomography image is not periodic, so a "semiperiodic" displacement is used here, which is performed as follows: when a walker gets out of the cubic simulation cell from one side, then it will come back from the opposite side. Take the direction x, for example, assuming the cell centered on the origin, the simulation cell size is 500×10^3 voxels; if $x\geq250$, then $x'=x-500$; if $x<-250$, then $x'=x+500$. If the new position (x',y,z) is occupied by the brine phase, then this displacement will be allowed, otherwise it will be canceled. We have tested this displacement condition on two discretized "random close packing (RCP)" media [30]. In the first one, the configuration of the boundary condition is periodic; in the other one, we take a random cubic subset that hence loses the periodic boundary conditions. We apply our semiperiodic displacement in the second RCP model. The simulation gives a tortuosity value of about 1.7, which is very close to the value in the periodic image of RCP, which is 1.6. As discussed before, the quasistatic capillary displacement simulation does not allow one to get a homogeneous brine distribution along the invading axis. In the framework used in the simulation, the self-diffusion is then characterized by a diagonal tensor with two equal components in the plane perpendicular to the invading axis. As in the experimental setup, we use these values to compute $D_{\text{self}}(t\to\infty)$,

$$F_f=\frac{1}{\Phi}\frac{D_{\text{bulk}}}{[D_{\text{self}}(t\to\infty)]_{S_w=1}}, \tag{6}$$

$$R_{\text{ind}}=\frac{1}{S_w}\frac{[D_{\text{self}}(t\to\infty)]_{S_w=1}}{[D_{\text{self}}(t\to\infty)]_{S_w<1}}. \tag{7}$$

B. Saturated pore network and *m* estimation

The first Archie law concerns the fully saturated pore network. Two possible ways are generally used to estimate the m exponent. First, the strict application of Eq. (1) yields $m\sim1.65$ for our sample. Second, we can look at a homologous series of porous samples and analyze the evolution of the formation factor with the porosity. Here, we choose a third way inspired by Ref. [38]. Having only one available 3D tomography image, we want to elaborate a simple scenario inducing a slight structural evolution of the pore network. Each evolution will be performed using either a mathematical erosion or a dilation with a structuring cubic element of 27 pixels [39]. At each step, we estimated the formation factor using a random-walk algorithm. Results are shown in Fig. 14. The best fit to an Archie law is

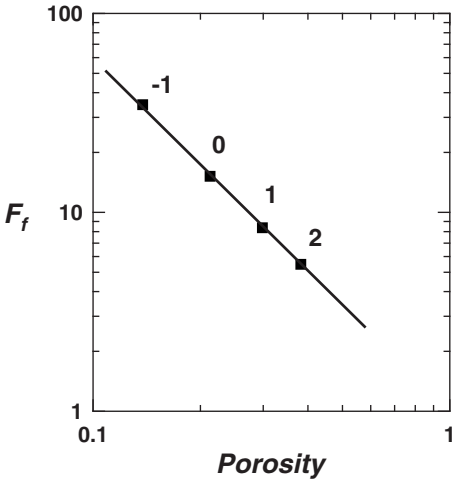

FIG. 14. Computation of the formation factor for a homologous series of saturated pore networks generated by a succession of mathematical erosion or dilation. The seed pore network is the 3D microtomography shown in Fig. 3. −1 stands for a first erosion. +1 stands for a first dilation. +2 stands for two consecutive dilations of the pore network. The straight line in log-log scale is the best fit according to the Archie law.

$$F_f=0.94/\phi^{1.81}. \tag{8}$$

We find an exponent $m=1.81$ higher than the estimation from Eq. (1) and slightly lower than experimental n exponent (1.9). Obviously, we have chosen a very simple way to mimic grain consolidation or pore network alteration. A more extended analysis using the same track is certainly needed to improve the numerical prediction.

C. Unsaturated pore network and disconnectedness process

For the R_{ind}-S_w curve computation, we have applied the random-walk simulation directly in the brine phase obtained by simulated annealing method and by "capillary displacement method." The dotted line in Fig. 15 represents the simulation results of the simulated annealing distribution and the continuous line shows the curve based on capillary displacement configuration. Both curves of these two brine distributions begin to diverge when the saturation diminishes below 0.2. This discrepancy is the consequence of the disconnectedness transition of the brine phase as discussed in Sec. IV C and localized in the vicinity of $S_w=0.12$ (see Fig. 13). We can observe that the R_{ind} divergence is more severe for the brine phase configuration obtained by capillary inva-

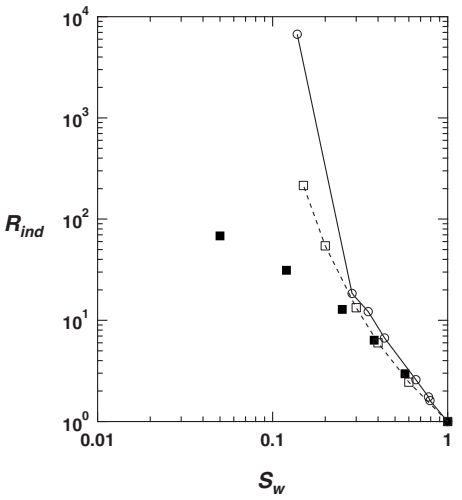

FIG. 15. Computed R_{ind}-S_w curves with brine phase configuration obtained either by simulated annealing or by capillary invasion and comparison with the experimental measurements. Black square: experimental measurements. White square: simulated annealing configuration. Circle: capillary displacement configuration.

sion. This is also in good agreement with the C evolution, shown in Fig. 13. As already said, the associated C evolution points to a less connected wetting phase all along the desaturation.

In both cases, the numerical divergence is certainly sensitive to the finite size of the observed pore network. For the simulated annealing, we have shown that the wetting fluid distribution, whatever the value of S_w, reaches a homogeneous distribution above a characteristic size ten time less than the system size (see Fig. 13). In such situation, the finite-size effect should be weak. This is certainly not the case for a fluid distribution obtained by quasistatic capillary displacement. In this situation and close to the disconnectedness transition, we have shown that the trapped regions within the span front exhibited a heterogeneous and/or a fractal structure on a length scale equivalent to the 3D reconstruction size (see Fig. 13). In both cases, the important result is the observation of a strong divergence of the resistivity index, incompatible with the experimental results at low saturation range. This disagreement points to the necessity to introduce a shortcut of the disconnectedness transition at low S_w.

D. Need for a wetting film at low S_w

The negative deviation observed in the measurement could be attributed to the electrical conduction of brine found in the capillary groove on the solid surface. When air invades a pore, brine is still trapped in the surface roughness due to high local capillary pressure; indeed, if we assume a radius of about 1 μm as a typical size of grooves at the surface, the capillary pressure necessary to empty these "pores" is about 1.4 bar, while the applied pressure was less than 500 mbar. This brine could form a continuous conduction path, called thick film [6]. Their thickness should be of the same order as the depth of the roughness. As a result, at low S_w, when the

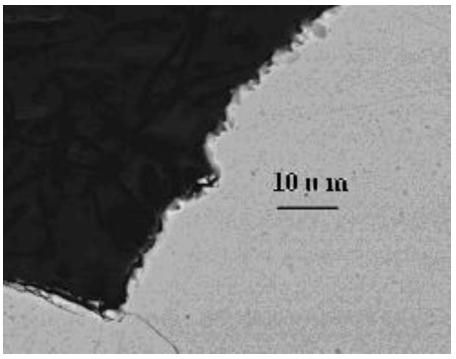

FIG. 16. Scanning electron microscopy image of grain surface roughness using backscattered electrons.

brine volume is below its disconnectedness threshold, the thick film could provide electrical conduction over the entire pore space, inducing a decrease in the resistivity index. An estimate of the average film thickness t can be made from the knowledge of the specific surface or more directly from the measured V/S ratio mentioned above. For example, at $S_w = 0.05$, $t \sim 0.3$ μm.

The surface roughness is imaged by SEM as shown in Fig. 16. We have estimated that the roughness depth is in the order of 1 μm. The influence of a thick film found on the solid surface was estimated numerically. For this aim, we added a layer of brine elements to the solid surface in the simulation. The thicknesses of this layer are 0.6 μm, of the same order as the roughness depth. To reproduce a film of 0.6 μm thick, all the voxels 3 μm in length (tomography image resolution) are divided into 5×10^3 identical subvoxels. As a result, each subvoxel is 0.6 μm in length. The rest of the work is to scan all the air voxels. If one of its six nearest neighbors belongs to the solid phase, then this air voxel is turned to a film voxel, as shown in Fig. 17.

The random-walk simulations are performed again in both the brine and film phase. The bulk diffusivity in these two phases is considered the same. Figure 18 shows the simulation results. This time, the simulation recovers the similar evolution of R_{ind}, as observed in the experiments. At the

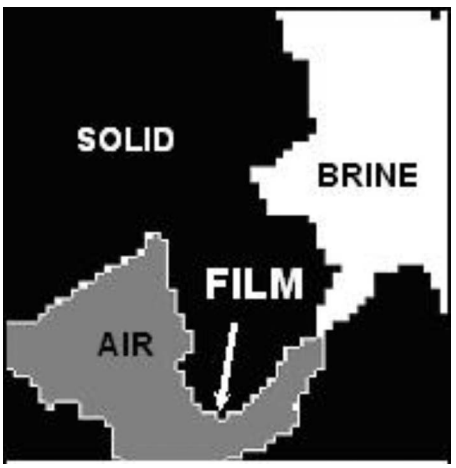

FIG. 17. Brine film configuration: the film elements cover the pore surface when the pore is emptied.

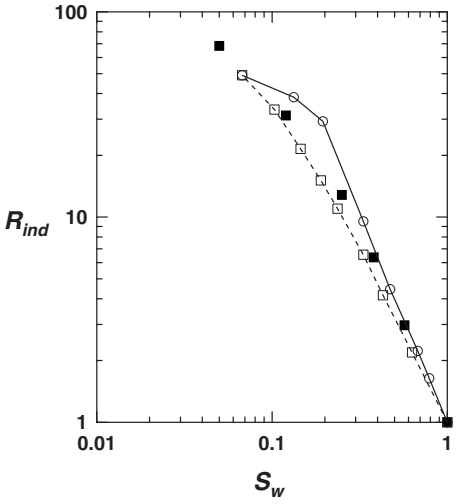

FIG. 18. Computed R_{ind}-S_w curves involving a thick film with a thickness equal to 0.6 μm. The last points (at small S_w) of the computed curves depend only on the resistivity of the film. Black square: experimental measurement. Open square: simulated annealing. Open circle: capillary displacement.

beginning of the drainage process, when the saturation value is greater than 0.2, the brine in pore volume percolates and dominates the electrical response. The simulation results of capillary displacement are in good agreement with the experimental measurement and follow a power law with an exponent value close to 1.9. The resistivity index curve of the simulated annealing fluid distribution is slightly underestimated. At low saturation range, when the brine in pore volume is below the percolation threshold and loses its electrical conduction connectivity, the brine thick film is still percolating all over the pore space, which guarantees the conduction continuity and becomes dominant to the resistivity of the system. In our simulation, with the presence of the thick film, the negative deviation appears for the two brine configurations. However, the capillary displacement shows a more steeply bending down trend, while the simulated annealing presents a change in the regime that is more comparable with the experimental observation.

VI. CONCLUSION AND PERSPECTIVE

The electric conductivity of a partially water-saturated clay-free sandstone was measured, and a strong negative deviation from the well-known Archie law was observed at low water saturation (S_w). This observation is attributed to the existence of a thick liquid film, assuring the ionic conduction at this saturation regime. A numerical simulation was used to confirm this scenario. Two protocols were proposed to distribute the brine phase in the pore network of a 3D microtomography image. The first one is based on a minimization of the interfacial energy; the second, takes into account the quasistatic capillary displacement. The classical random-walk algorithm was used to compute the formation factor and the resistivity index at various water saturations. Without the thick film, both of the two fluid-placing protocols show a disconnectedness transition when $S_w < 0.2$. Adding this "film" to the solid surface, the electrical continuity is maintained and the bending down trend is reproduced in our simulations. The simulated annealing method describes well the menisci configuration at the grain contacts as well as gives a fluid configuration that is more realistic in the low S_w range. It is the reason why the R_{ind}-S_w curves with the simulated annealing give better simulation results when $S_w < 0.4$.

ACKNOWLEDGMENTS

We are grateful to N. Gland for his valuable suggestions. We acknowledge also S. Gautier and A. Samouillet for their kindness and technical supports. This research is supported by a CIFRE CNRS-IFP grant. Grants from ANR projects MIPOMODIN and DYOPTRI are acknowledged.

[1] G. E. Archie, Trans. AIME **146**, 54 (1942).
[2] H. N. Edmundson, Tech. Rev.- Mitsubishi Heavy Ind. **36**, 12 (1988).
[3] G. W. Anderson, J. Pet. Technol. **37**, 1125 (1986).
[4] B. Berkowitz and D. P Hansen, Trans. Porous Media **45**, 301 (2001).
[5] R. Lenormand and C. Zarcone, J. Fluid Mech. **135**, 337 (1983).
[6] F. A. L. Dullien, *Porous Media*, 2nd ed. (Academic Press, New York, 1992).
[7] P. Spanne, J. F. Thovert, C. J. Jacquin, W. B. Lindquist, K. W. Jones, and P. M. Adler, Phys. Rev. Lett. **73**, 2001 (1994).
[8] D. A. Coker, S. Torquato, and J. H. Dunsmuir, J. Geophys. Res. **101**, 17497 (1996).
[9] L. M. Schwartz and J. R. Banavar, Phys. Rev. B **39**, 11965 (1989).
[10] L. M. Schwartz, Physica A **207**, 28 (1994).
[11] P. Levitz, Adv. Colloid Interface Sci. **76-77**, 71 (1998).
[12] M. Fleury, Proceedings of the International Symposium of the Society of Core Analysts, Canada, SCA-35, 2007 (unpublished).
[13] M. Han, M. Fleury, and P. Levitz, SCA, Proceedings of the International Symposium of the Society of Core Analysts, Canada, SCA-34, 2007 (unpublished).
[14] M. Fleury, Proceedings of the International Symposium of the Society of Core Analysts, Netherlands, SCA-9833, 1998 (unpublished).
[15] A. Birovljev, L. Furuberg, J. Feder, T. Jøssang, K. J. Måloy, and A. Aharony, Phys. Rev. Lett. **67**, 584 (1991).
[16] H. Auradou, K. J. Maloy, J. Schmittbuhl, A. Hansen, and D. Bideau, Phys. Rev. E **60**, 7224 (1999).
[17] H. F. Dunlap, Trans. Am. Inst. Min., Metall. Pet. Eng. **186**, 259 (1949).
[18] K. M. Diederix, Transactions of the SPWLA 23rd Annual Logging Symposium, Corpus Christi, Texas, 1982, Paper X (unpublished).

[19] S. Kirkpatrick, C. D. Gelatt, and M. P. Vecchi, Science **220**, 671 (1983).
[20] R. Knight, A. Chapman, and M. Knoll, J. Appl. Phys. **68**, 994 (1990).
[21] D. L. Silverstein and F. Fort, Langmuir **16**, 839 (2000).
[22] N. Metropolis, A. Rosenbluth, M. Rosenbluth, A. Teller, and E. Teller, J. Chem. Phys. **21**, 1087 (1953).
[23] F. A. L. Dullien, C. Zarcone, I. F. MacDonald, and R. D. E. Bochard, J. Colloid Interface Sci. **127**, 362 (1989).
[24] D. Wilkinson and J. F. Willensem, J. Phys. A **16**, 3365 (1983).
[25] R. Lenormand and C. Zarcone, Phys. Rev. Lett. **54**, 2226 (1985).
[26] C. E. Diaz, I. Chatzis, and F. A. L. Dullien, Transp. Porous Media **2**, 215 (1987).
[27] I. Fatt, Pet. Trans. AIME **207**, 160 (1956).
[28] S. Youssef, E. Rosenberg, N. Gland, and S. Bekri, Proceedings of the International Symposium of the Society of Core Analysts, Canada, SCA-17, 2007 (unpublished).
[29] L. Xu, S. Davies, A. B. Schofield, and D. A. Weitz, Phys. Rev. Lett. **101**, 094502 (2008).
[30] P. Levitz, J. Phys. Chem. **97**, 3813 (1993).
[31] L. K. Barrett and C. S. Yust, Metallography **3**, 1 (1970).
[32] C. Lin and M. H. Cohen, J. Appl. Phys. **53**, 4152 (1982).
[33] J. Y. Arns, V. Robins, A. P. Sheppard, R. M. Sok, W. V. Pinczewski, and M. Knackstedt, Transp. Porous Media **55**, 21 (2004).
[34] L. Pothuaud, P. Porion, E. Lespessailles, C. L. Benhamou, and P. Levitz, J. Microsc. **199**, 149 (2000).
[35] K. R. Mecke and H. Wagner, J. Stat. Phys. **64**, 843 (1991).
[36] A. P. Roberts and M. Teubner, Phys. Rev. E **51**, 4141 (1995).
[37] J. Jouannot, J. P. Jernot, and E. Guyon, C. R. Acad. Sci., Ser. IIb: Mec., Phys., Chim., Astron. **321**, 425 (1995).
[38] J. N. Roberts and L. M. Schwartz, Phys. Rev. B **31**, 5990 (1985).
[39] J. Serra, *Image Analysis and Mathematical Morphology* (Academic, London, 1982).
[40] N. Morrow, Ind. Eng. Chem. **62**, 32 (1970).